

Supporting Information

Ruf et al. 10.1073/pnas.1616019114

SI Materials and Methods

ICP-MS Experiments. Methanolic extracts and residues of the meteorites were analyzed for total elemental composition. Extracts were diluted appropriately 10- or 26-fold to achieve the necessary sample volume. Extract residues were pressure-digested. Samples were exactly weighed within quartz vessels, to which 1 mL HNO₃, Suprapur, subboiling distilled (Merck), was added. The vessels were closed and introduced into a pressure digestion system (Seif) for 10 h at 170 °C. The resulting clear solutions were filled up exactly to the mark at 10 mL with Milli-Q H₂O and were then ready for element determination.

An ELEMENT 2 Thermo-Electron inductively coupled plasma sector field mass spectrometry instrument was used for determination of the elements. A solution of ¹⁰³Rh was added as an internal standard to each sample at a concentration of 1 µg/L. Sample introduction was carried out using a peristaltic pump connected to a Meinhard nebulizer with a cyclon spray chamber. The rf power was adjusted to 1,300 W, the plasma gas was 15 (L Ar)/min, whereas the nebulizer gas was ~0.9 (L Ar)/min after daily optimization. Measured element isotopes were as follows: ⁹Be, ¹¹⁴Cd, ⁵⁹Co, ⁵²Cr, ⁵⁶Fe, ²⁰²Hg, ¹⁹³Ir, ⁵⁵Mn, ⁹⁸Mo, ⁶⁰Ni, ²⁰⁸Pb, ¹²¹Sb, ⁷⁸Se, ⁵¹V, and ¹⁸⁴W.

Each determination method has been validated previously by regular laboratory intercomparison studies and by regular analyses of adequate certified reference materials, the latest directly before this study. Routinely, every 10 measurements, three blank determinations and a control determination of a certified standard for all mentioned elements were performed. Calculation of results was carried out on a computerized laboratory-data management system, relating the sample measurements to calibration curves, blank determinations, control standards, and the weight of the digested sample.

The solid-state meteorite sample was scanned using a commercial laser ablation system coupled to inductively coupled plasma mass spectrometry (LA-ICP-MS). The laser ablation system was a NWR 213 instrument from New Wave Research/ESI, equipped with a beam expander, yielding laser spot sizes between 4 and 250 µm. The laser system was coupled to a PerkinElmer NexIon 300 ICP-mass spectrometer (Sciex). The ICP-MS was synchronized with the LA unit in external triggering mode. The meteorite piece was mounted into the standard sample cell of the LA system with laboratory plasticine between the sample holder and the lower side in such a way that the flat upper side surface of the meteorite was placed on a level, where the laser would be focused. The exact position for ablation lines was defined by using the dual microscope of the LA system. The laser settings were as follows: energy, 30 J/cm²; power output, 100%; pulse repetition rate, 10 Hz; scan speed, 20 µm/s; spot size, 100 µm; and ablation pattern, lines. The Ar-gas flow to ICP-MS was 1.14 L/min. The ICP-MS settings were as follows: rf power, 1,200 W; plasma gas, 15 (L Ar)/min; and dwell time per isotope, 15 ms. The following isotopes have been selected for analysis: ²⁴Mg, ²⁷Al, ²⁸Si, ³⁵Cl, ⁵¹V, ⁵⁵Mn, ⁵⁷Fe, ⁵⁹Co, ⁶⁰Ni, ⁶³Cu, ⁶⁶Zn, ⁹⁸Mo, and ¹³⁸Ba. ICP-MS data were exported to Microsoft Excel, where signal intensities were color-coded.

SIMS Experiments. Measurements were performed using an IMS-4f Cameca secondary ion mass spectrometer. Etching in oxygen plasma for 10 min was performed to remove carbon contamination on the sample surface after grinding and polishing. These

conditions were used to study a glassy vein of Chelyabinsk meteorite as selected target.

The sample target is a good insulator and charged during analysis. A normal incidence electron gun was used to compensate the positive charge on the sample surface. This gun has been effectively applied to detect negative secondary ions. In this case, the field accelerating the secondary ions was decelerating for electrons and therefore a cloud of electrons was created above the sample surface. This cloud discharges the charging areas of the sample surface, which was coated additionally with thin a layer of gold (~10 nm) to improve the discharge.

Because negatively charged secondary ions were selected for analysis, it was necessary to provide a high yield. This technique is well-known and consists of using Cs⁺ as the primary ions with impact energy of 14.5 keV to ablate analyte atoms/molecules. In contrast to the positive secondary ions, the detection of negative secondary ions has its own characteristics. Not all chemical elements have strong electron affinity. For example N, Ca, Mn, and Mg have electron affinity values close to zero. However, the analyzed sample was a mixture of oxides. To determine the elements of these oxides, molecular ions of MgO⁻ as well as C⁻, H⁻, and Si⁻ ions were detected and mapped.

Mass spectral resolution of 5,000 was used to overcome interference problems. The map of element distributions was performed using a dynamic transfer system. Lateral resolution was determined by the field-of-view aperture and equals 5 µm with a raster of 250 × 250 µm. Output data of the SIMS results were the signal intensities at the coordinates (x, y) analysis at a certain depth. The software, using the obtained coordinates and the intensities of the analyzed element signal, allows visualizing the data as a 2D distribution, where each point is assigned as a color depending intensity at that point.

ESI-FT-ICR-MS Experiments: Instrumental Details. The experimental study was performed on a high-field FT-ICR mass spectrometer from Bruker Daltonics with a 12-T magnet from Magnex. A time-domain transient with 4 MWords was obtained and Fourier-transformed into a frequency domain spectrum. The frequency domain was afterward converted to a mass spectrum by the solariX control program of Bruker Daltonics. The ion excitations were generated in broadband mode (frequency sweep radial ion excitation) and 3,000 scans were accumulated for each mass spectrum in a mass range of 147–1,000 amu. Ions were accumulated for 300 ms before ICR ion detection. The pressure in the quadrupole/hexapole and ICR vacuum chamber was 3 × 10⁻⁶ mbar and 6 × 10⁻¹⁰ mbar, respectively. For CID-MS/MS, ions were accumulated for 3 s.

The ESI source (Apollo II; Bruker Daltonics) was used in negative ionization mode. The methanolic solutions were injected directly into the ionization source by means of a microliter pump at a flow rate of 120 µL·h⁻¹. A source heating temperature of 200 °C was maintained and no nozzle-skimmer fragmentation was performed in the ionization source. The instrument was previously externally calibrated by using arginine negative cluster ions (5 mg·L⁻¹ arginine in methanol).

FT-ICR mass spectra with *m/z* from 147 to 1,000 amu were calibrated externally and internally to preclude alignment errors. Subsequently, the mass spectra were exported to peak lists at a signal-to-noise ratio ≥3. Elemental formulas were calculated combinatorially within a mass accuracy window of ±0.2 ppm for

each peak in batch mode by an in-house software tool and validated via the senior-rule approach/cyclomatic number (45), assuming valence 2 for S and valence 4 (coordination number) for Mg. Following senior's rules, twofold-coordinated Mg(II) resulted in invalid molecular formulas, which were excluded for further data evaluation.

Computations. The electronic structure simulations were performed on a stand-alone computer by ab initio quantum mechanical computations, based on density functional theory (DFT), as implemented in Gaussian 03 (46). The hybrid DFT-functional B3LYP was implemented with d-polarization functions for each heavy atom and 1p for each hydrogen atom in all single-point energy calculations. All geometry optimizations were performed with the 6-31+G(d,p) basis set. Frequency calculations were done for each optimized geometry with the same 6-31+G(d,p) basis set to obtain the zero-point vibrational energy. This value was multiplied by a scaling factor of 0.9804 to correct for vibrational anharmonicities (47). Another intention for performing the frequency analysis is the identification of transition states. Detecting negative frequencies (imaginary frequencies) implies that the optimized geometry is not fully relaxed as a stationary point on the potential energy surface. The single-point energy calculations were done at the 6-311+G(2d,p) level of theory. The use of diffuse functions was important to represent the correct geometry and thermodynamic properties of anionic species (48). Stability tests were performed in critical cases (significantly different energy values relative to the homologous series of treated attachment systems) to ensure that the used wave function represents the lowest energy solution of the self-consistent field equations.

For geometry optimization, the Berny analytical gradient optimization routines (49, 50) were used in combination with the GDIIS algorithm (51). The requested convergence value in the density matrix was 10^{-8} , the threshold value for maximum displacement was 0.0018 Å, and the threshold value for the maximum force was 0.00045 Hartree Bohr⁻¹. The nature of the stationary points was established by calculating and diagonalizing the Hessian matrix (force-constant matrix). All geometries of electronic structures calculated were viewed with the GaussView or Avogadro program.

The Gibbs free energy ΔG between each neutral Mg(OH)₂ and the anionic carboxylate anion in the gas phase was calculated with Eq. S1, satisfying the reaction of Eq. 1:

$$\Delta G = -BE = E(\text{Complex}) - (E(\text{Mg(OH)}_2) + E(\text{RCOO}^-)). \quad [\text{S1}]$$

$E(x)$ are the single-point energies of respective species x and R = hydrocarbon C_xH_y with $x, y \in \mathbb{N}$. Therefore, the two educts were first optimized in the absence of the reaction partner (step 1). Afterward, the charged complex was relaxed (step 2). The mentioned energies in Eq. S1 are the single-point energies of steps 1 and 2. All computations are referred to gas-phase conditions.

Correlation Between the Experimental and Computed Fragmentation Energies. The minimum collision energy of 10 eV, required to initiate dissociation of the C₁₆-dihydroxymagnesium carboxylate complex anion, had to be scaled because the magnitude of internal energy deposition from kinetic acceleration in an electric field in a quadrupole can be estimated to reach 20% (52). The corresponding energy of 193.3 kJ/mol is in the range of the DFT-computed binding energy (BE) for [(OH)₂MgO₂CR][−] for the reaction of Mg(OH)₂ with the carboxylate anion ($BE_{\text{computed}} = 206.7$ kJ/mol).

Calculation of the Measured Equilibrium Constant K' . The equilibrium constant K for the reaction in Eq. 1 is given as

$$K = \frac{a([(OH)_2MgO_2CR]^-)}{a(RCOO^-) \cdot a(Mg(OH)_2)} \approx \frac{c([(OH)_2MgO_2CR]^-)}{c(RCOO^-) \cdot c(Mg(OH)_2)} \quad [\text{S2}]$$

with R = hydrocarbon C_xH_y with $x, y \in \mathbb{N}$. Thermodynamic activities $a(x)$ can be approximated by concentrations $c(x)$ for different molecules x , when ideal behavior is assumed. $c(x)$ is expressed as the compound's mass spectrometric intensity I , which is proportional to the compound's abundances (53). For K , a measured equilibrium constant K' is used with the assumption that $c(Mg(OH)_2) \gg c(RCOO^-)$ because of the much higher amount of mineral compounds relative to the organic compounds (54). Therefore, the reaction is considered as a pseudo-first-order reaction, where $d(c(Mg(OH)_2))/dt \sim 0$. Thus, K' is calculated with Eq. S3 instead:

$$K' = \frac{I([(OH)_2MgO_2CR]^-)}{I(RCOO^-)}. \quad [\text{S3}]$$

Mass Difference Network Reconstruction. Theoretical ion masses of the above assigned molecular formulas were used for mass difference network reconstruction. Theoretical ion masses (nodes) were connected by edges if their mass differences were equal (± 0 ppm) to the theoretical mass differences of ΔCH_2 (14.015650 amu), ΔO (15.994915 amu), or $\Delta Mg(OH)_2$ (57.990521 amu). Mass difference networks were laid out using the Cytoscape software (Allegro version 3.2.1 layout) (55).

Statistical Evaluation of Meteorite Samples. CHOMg mass lists were aligned with an in-house software (56). To stabilize the variance, only m/z values present in more than 5% of all samples were further considered in the statistical elaboration to remove unique compounds. The peak intensities were scaled to unit variance and logarithm-transformed.

To evaluate the data, several multivariate models were set up. Orthogonal partial least square discriminant analysis (OPLS-DA) and OPLS regression models were performed by the sevenfold cross-validation procedure, as implemented in the software SIMCA, and then verified with CV-ANOVA (cross-validation ANOVA), to exclude overfitting. Relevant indicators, such as P value, $R^2(Y)$, and $Q^2(\text{cum})$, were subsequently reported to indicate the significance, the goodness of the fit, and the quality of the model prediction. Moreover, potential discriminating variables were chosen by examining the loading plot. The software tools, used for the statistical elaboration, were SIMCA 13.0.3.0 (Umetrics) and RStudio (version 0.98.1103; RStudio, Inc.).

First, a classification model was set up via OPLS-DA using a meteorite subset, formed by samples with assigned information about their thermal stress level. All samples were correctly classified with a Fisher probability of $5e^{-81}$ and the model was valid ($P < 0.001$). Based on this model, properties were predicted for additional samples without any available thermal stress information. Based on the classification, a gradient for the thermal stress was set up among all samples from low- to high-thermally stressed meteorites. This gradient was used as Y variable in an OPLS model to reveal a possible relation between the m/z variables and Y . The OPLS score scatter plot (Fig. 5) was robust to overfitting ($P = 0.004$) with $R^2(Y) = 0.91$ and $Q^2(\text{cum}) = 0.27$. The ellipse represents the Hotelling's T^2 confidence region (95%). The first axis (x axis) is the so-called first component with the new samples coordinate. It can be seen as the best-fit line that traverses the geometric origin of the dataset accounting for the greatest amount of variance of the data. The second greatest variance is explained by the second component, orthogonal to the first, and so on. All of the components have to be uncorrelated each other and cumulatively all together account for the 100% of the variance. The aforementioned coordinates of data points on

the first component are the first principal component values, or component scores; they are computed as the product of (centered) data matrix and the eigenvector.

The most relevant masses, 50th percentile of loading values of the y axis (oxygen variation in CHOMg formulas), were visualized in modified van Krevelen diagrams, as depicted in Fig. 5. Concerning the thermal stress variation, the most relevant masses, 50th percentile of loading values of the x axis, were visualized in modified van Krevelen diagrams, as depicted in Fig. S6. The box plot was set up by counting CHOMg formulas for negative and positive loading values on the x axis, respectively.

Hierarchical cluster analysis (HCA) was performed using the average linkage method (UPGMA) for the distance between clusters and the Pearson correlation coefficient as criteria to cluster the variables. The HCA was done by the Hierarchical Clustering Explorer 3.0 (Human-Computer Interaction Lab, University of Maryland). Hierarchical cluster analysis organizes the samples, as a graphical output, into a dendrogram (cluster tree) whose branches are the desired clusters. Based on different similarity rules the clusters are defined. Similar samples are within a cluster.

Mg Isotope Measurements. All samples (both the methanolic extracts and residues) were dissolved subsequently using a standard 3:1 HF:HNO₃ dissolution technique in Savillex 3-mL vials (hexagonal cap, square body type) (57). After dissolution, *ca.* ~1% aliquot of the solution was saved for ²⁷Al/²⁴Mg analyses. The remainder was centrifuged and processed through a cation exchange column to separate Mg from the sample matrix and potential isobaric interferences. The column procedure was first calibrated to separate Mg from matrix elements, such as Na, Al, K, and Ca. In particular, separation of Mg and Ca is important because this has been shown to cause fractionation of Mg isotope ratios by up to 1‰ (58). Standards and unknowns were dried down (~20 µg of Mg) and redissolved in 0.5 mL of 1 N HNO₃ before eluting through 0.75 mL of BioRad AG50W-X12 resin (200–400 mesh). We added a rinse step involving 3 mL of 0.15 M HF, which causes removal of Al and Ti from the column but leaves Mg unaffected. The Mg cut was collected in 12 mL of 1 N HNO₃. Once eluted, the Mg fraction was collected and dried

down and the residue was redissolved in 20 µL of concentrated HNO₃ to oxidize any organic molecules derived from the resin. After repeating this column chemistry, the final Mg fraction was dried down and redissolved in 1 mL of 2% HNO₃. After sample processing, the resin was cleaned by repeated elutions of 7 M double-distilled HNO₃ and Milli-Q ultrapure H₂O. Both Mg isotope compositions and ²⁷Al/²⁴Mg ratios were measured on a Thermo Neptune Plus HR-MC-ICP-MS in the Department of Earth and Planetary Sciences at the University of California, Davis.

Isotopic analyses of Mg were bracketed using the DSM-3 pure Mg standard (59) to account for instrumental mass bias and drift throughout the analysis period. Mg isotope ratios are expressed using delta notation as parts per thousand (‰) differences from DSM-3. Each sample was initially prescreened using 1% of the final Mg solution to ensure accurate dilution of the sample to match the signal intensity of the bracketing standard to within 10%. Samples were analyzed under dry plasma conditions using an ESI Apex IR desolvating nebulizer, which suppresses oxide interferences. The samples were analyzed in medium resolution to avoid the CN⁺ peak on ²⁶Mg, which cannot be resolved at low resolution. Using a high-sensitivity “x” skimmer cone the typical intensities for a 500-ppb solution at medium resolution were between 20–25 V of ²⁴Mg (amplified with a 10¹¹-ohm register board). Blank intensities on ²⁴Mg were typically 0.003–0.005 V.

To assess the accuracy of our measurements, the pure Mg standard CAM-1 was routinely measured throughout each analytical session. In total, CAM-1 was measured 78 times with an average $\delta^{26}\text{Mg}$ value of -2.61 ± 0.08 ‰, which is within error of the accepted value (-2.59 ± 0.14 ‰) (59). To assess the accuracy of the column chemistry and our external reproducibility, the USGS basalt standard BCR-2 was processed with every batch of column chemistry. A total of 26 separate analyses from eight separate chemical separations were performed on this standard. On average, BCR2 had a $\delta^{26}\text{Mg}$ value of -0.20 ± 0.07 ‰ and $\delta^{25}\text{Mg}$ value of -0.10 ± 0.04 ‰, which is within error of the estimated average composition of the upper continental crust ($\delta^{26}\text{Mg} = -0.22$ ‰) (60) and other recent published values for basalts (61).

Experiment Simulation

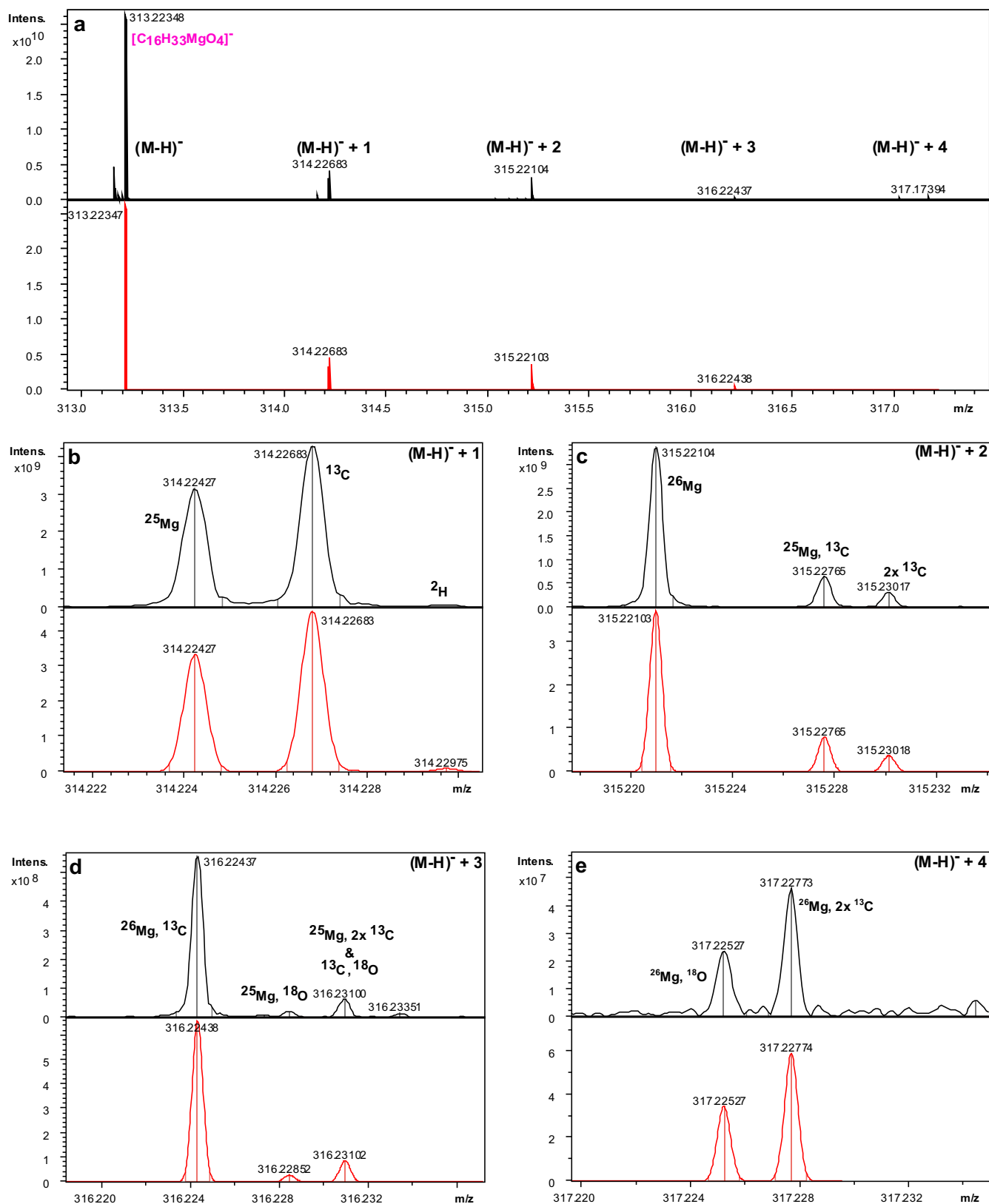


Fig. S2. (A–E) Isotopic fine structure for the $[C_{16}H_{33}MgO_4]^-$ molecule ion. $[C_{16}H_{33}MgO_4]^-$ was identified via its isotopologues in the Novato methanolic extract, as seen in ESI-FT-ICR mass spectra. The black spectrum is the experimental mass spectrum from Novato extract, and the red profile represents the theoretically computed isotopic pattern at natural abundance of C, H, O and Mg. The observed isotopic distribution is primarily caused by the isotopes $^{24/25/26}\text{Mg}$, $^{12/13}\text{C}$, $^{16/18}\text{O}$ and ^1H . To separate each isotopologue at FWHM, a minimum mass resolving power of $R \sim 125,000$ at $m/z = 313$ is required. Beyond CHOMg, the total combinatorial molecular complexity within the sample set includes N and S compositions. The mass resolving power of $R \sim 500,000$ helps to exclude more complex combinatorial formula solutions, which contain, for example, nitrogen and sulfur and discriminates unambiguously the CHOMg from the CHNOS chemical compositions.

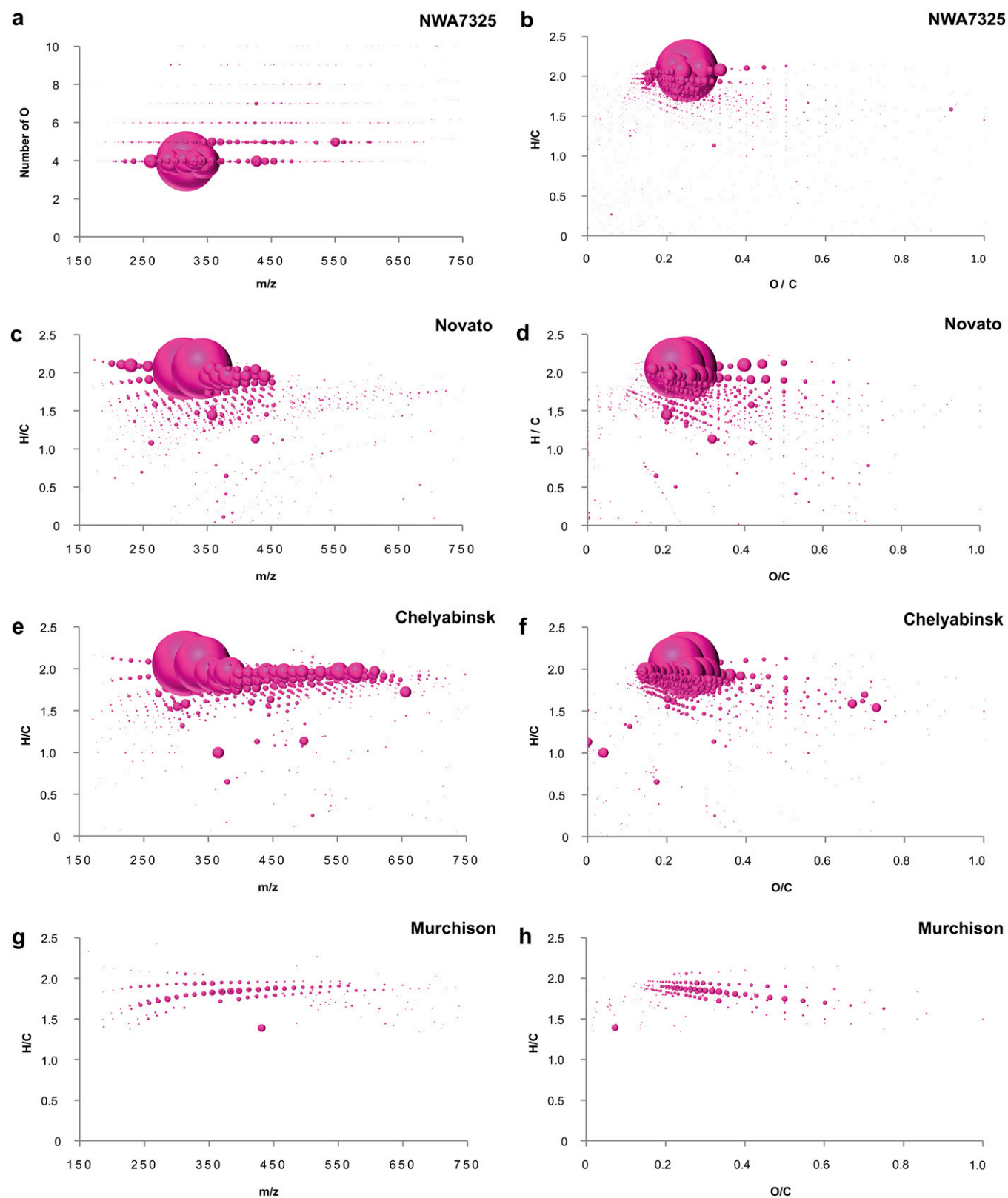


Fig. S3. Complexity of the CHOMg chemical space. (A) The dominance of CHOMg molecules possessing four oxygen atoms compared with the whole CHOMg chemical space for the soluble organic matter of NWA 7325. H/C vs. O/C for NWA 7325 (B), H/C vs. O/C and H/C vs. m/z representations of CHOMg chemical compositions for Novato (C and D), Chelyabinsk (E and F), and Murchison (G and H) meteorite samples illustrate the chemical complexity of their organic extracts. The bubble size represents the relative intensity of the mass peaks. The mass-edited H/C ratio diagram of NWA 7325 is shown in Fig. 2A in the main text.

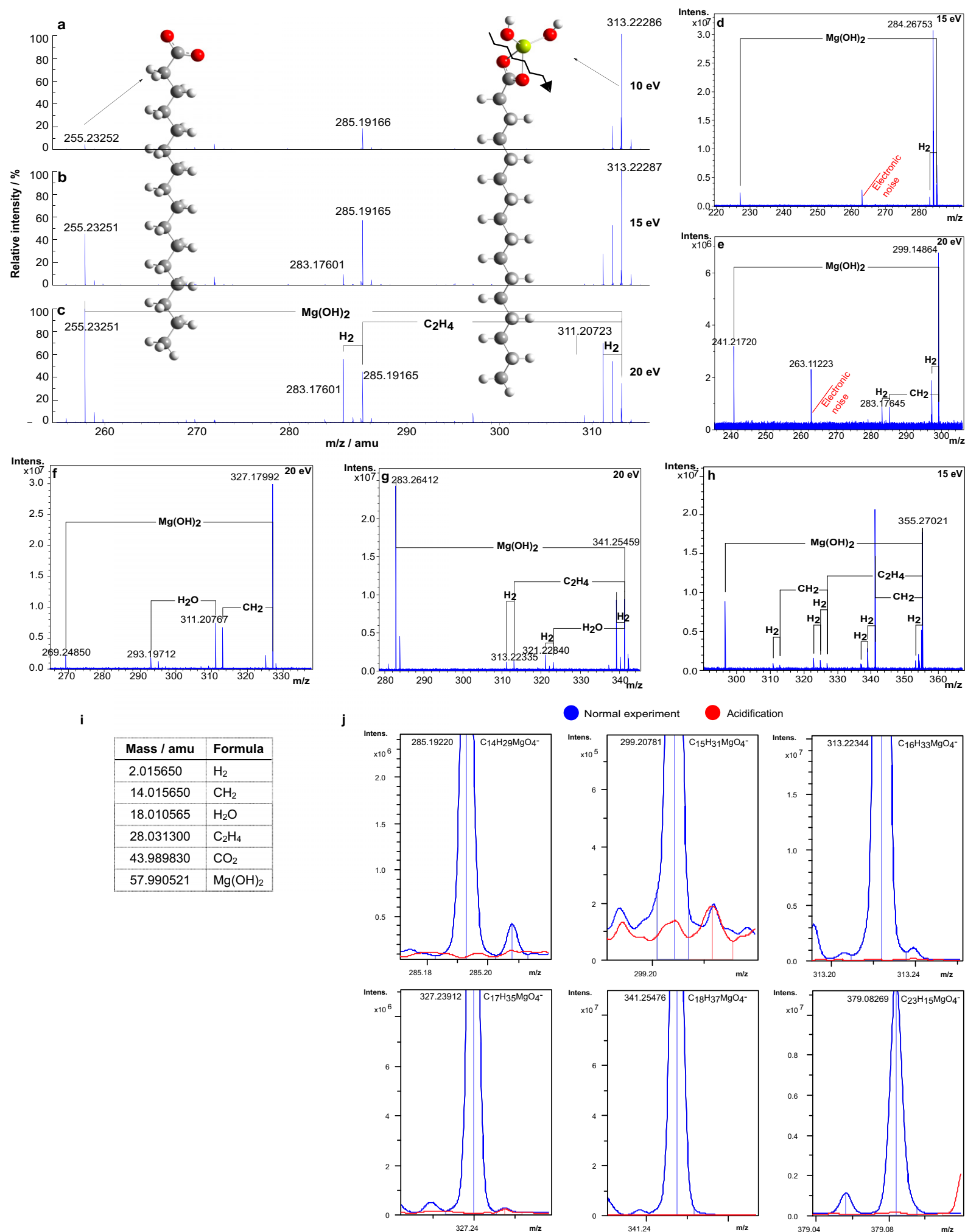


Fig. S4. Fragmentation experiments to characterize dihydroxymagnesium carboxylates. (A–C) CID mass spectra of NWA 7325 of C₁₆-dihydroxymagnesium carboxylate [C₁₆H₃₃MgO₄]⁻ complex are shown at collision energies of 10 eV, 15 eV, and 20 eV to identify the MgO₄R⁻ structures with R = hydrocarbon C_xH_y and x, y ∈ ℕ. Additionally, five precursor molecular ions, m/z = 285 for [C₁₄H₂₉MgO₄]⁻ (D), m/z = 299 for [C₁₅H₃₁MgO₄]⁻ (E), m/z = 327 for [C₁₇H₃₅MgO₄]⁻ (F), m/z = 341 for [C₁₈H₃₇MgO₄]⁻ (G), and m/z = 355 for [C₁₉H₃₉MgO₄]⁻ (H) show fairly congruent fragmentation patterns of dihydroxymagnesium carboxylates with the release of Mg(OH)₂ out of the fragmented parent molecule. The collision energies used in these CID MS/MS experiments were high (15–20 eV) to ensure fragmentation of the complexes. The computed coordinates of the structures of C₁₆-dihydroxymagnesium carboxylate ([C₁₆H₃₃MgO₄]⁻) and its product ion (hexadecanoic acid) are presented in Table S2. (I) Exact masses of the fragmented molecules. (J) Negative ionization mode ESI-FT-ICR mass spectra of selected dihydroxymagnesium carboxylates [(OH)₂MgO₂CR]⁻ in the NWA 7325 methanolic extract are shown, where the standard extract is labeled blue and the red signal is the extract in presence of formic acid (HCOOH). The complex is hydrolyzed in the presence of formic acid and Mg(OH)₂ is precipitated. This indicates that the CHOMg anionic complexes possess Mg(OH)₂ functional groups. The peaks were smoothed via the Gauss smoothing algorithm, as implemented in Bruker Compass DataAnalysis 4.2 SR1, with a smoothing width of 0.001 amu (2.1 points).

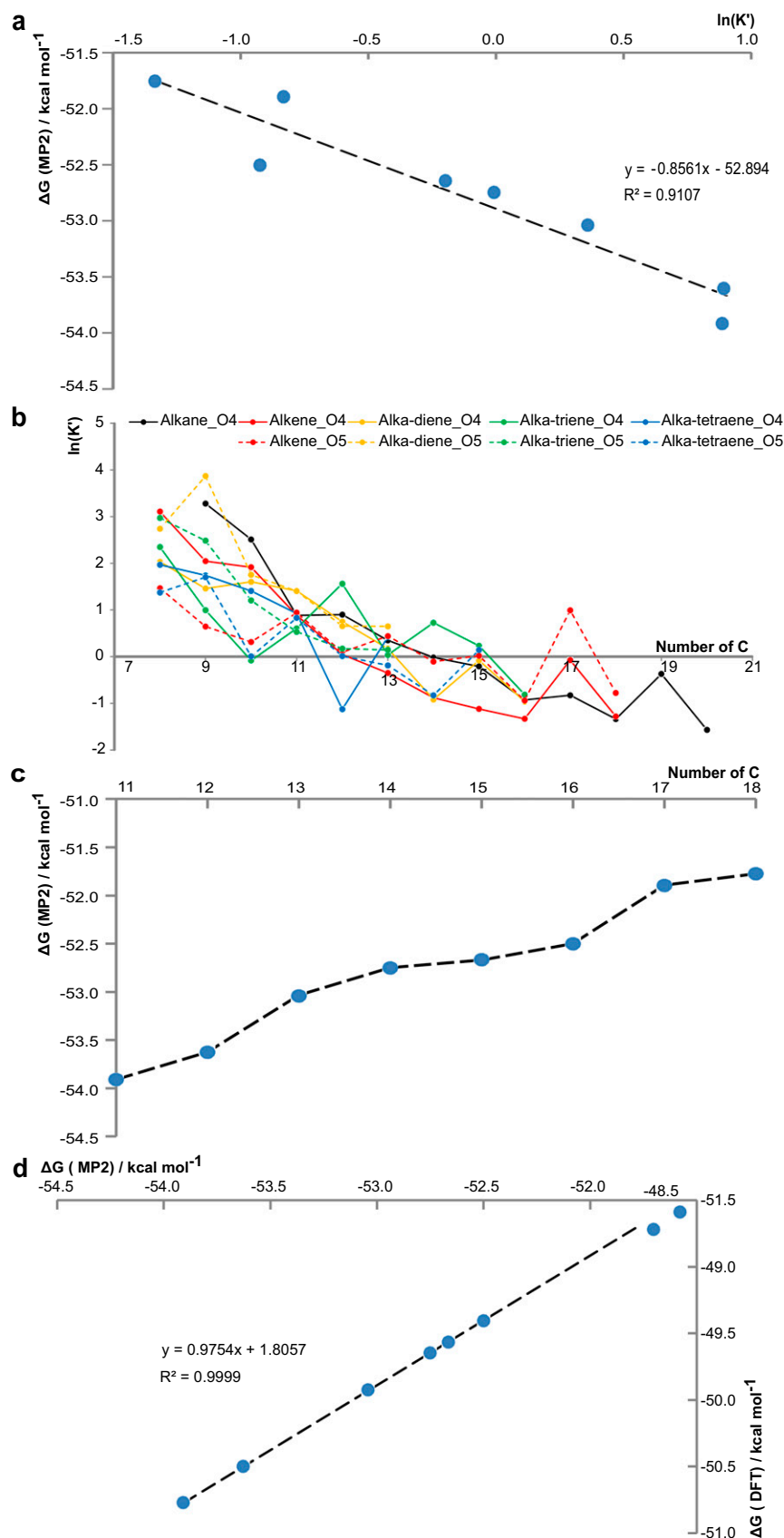


Fig. S5. General CHOMg reactivity and verification of DFT simulations with MP2 level of theory. (A) Negative correlation of the Gibbs free energy ΔG with $\ln(K')$, following Eq. 2 for different linear alkyl chain lengths between C_{11} and C_{18} , computed with MP2 extracts (discussed in the main text). (B) $\ln(K')$ is plotted vs. the number of carbon atoms for several homologous series, varying by alkyl saturation and number of oxygen atoms in the aliphatic chain. A general decreasing trend with increasing numbers of C atoms is observed, indicating that smaller alkyl chain CHO molecules are more reactive to form CHOMg compounds, relatively longer aliphatic chain molecules. Additionally, local reactivity anomalies are highlighted by functional fluctuations. (C) ΔG is plotted vs. the number of carbon atoms in linear alkyl chain lengths of the $[(OH)_2MgO_2CC_n]^-$ complex formation with $n \in \mathbb{N}$, as computed on MP2-level of theory. (D) Correlation between the DFT-B3LYP and MP2 methods, which illustrates the accuracy of DFT, describing this complex formation reaction properly.

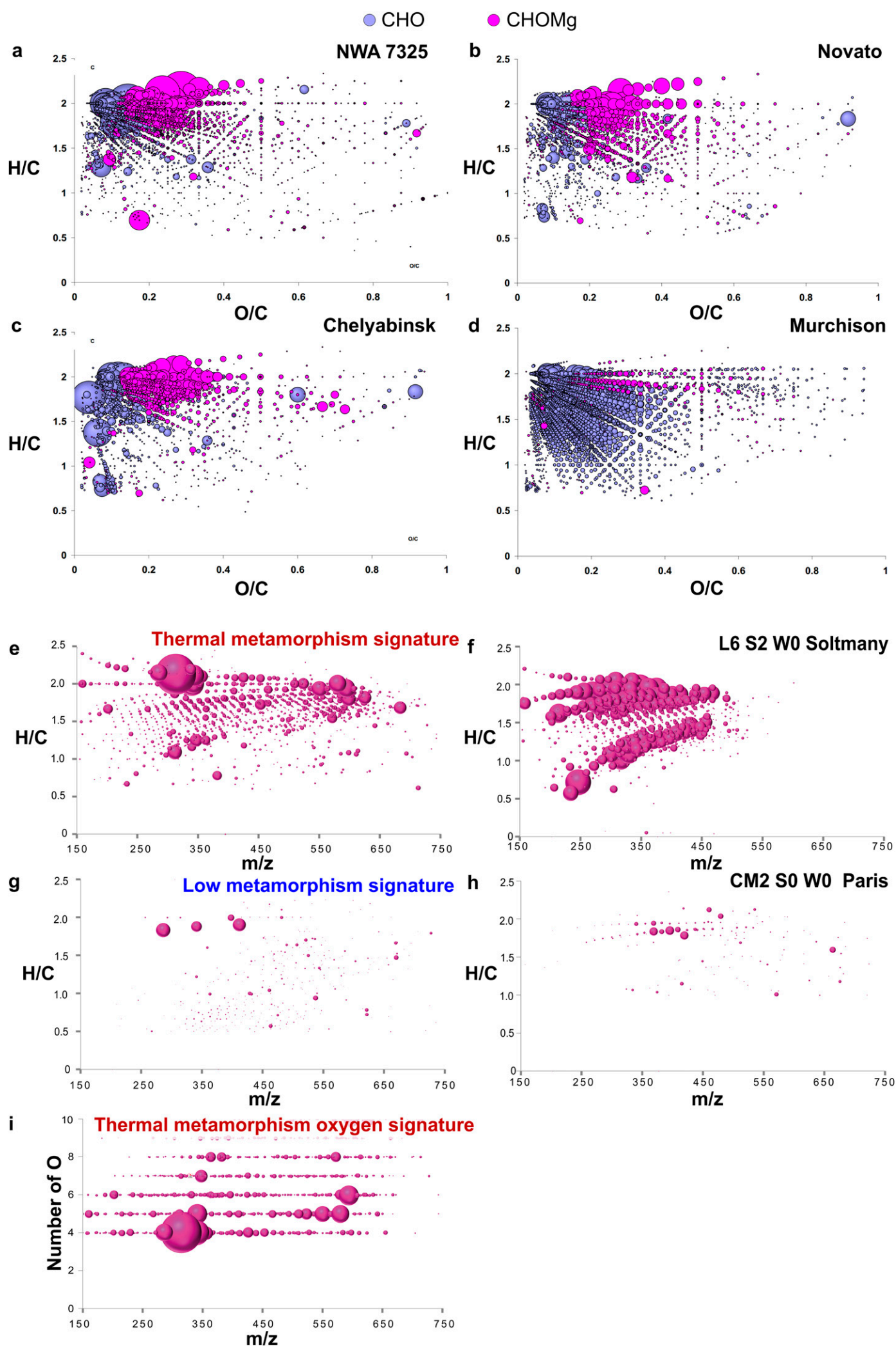


Fig. S6. Van Krevelen diagrams for the comparison of CHO and CHOMg compositions for several meteorites and modified van Krevelen diagrams representing the thermal metamorphism signature. Van Krevelen representations of soluble organic matter in NWA 7325 (A), Novato (B), Chelyabinsk (C), and Murchison (D) are shown. It is obvious that the less-altered CM2 chondrite Murchison is poor in CHOMg compositions, compared with the ungrouped achondrite NWA 7325 and the ordinary chondrites, Novato and Chelyabinsk. Modified van Krevelen diagrams of the overlapped CHOMg molecules (50th percentile of positive loading values on the x axis) reflect the highly aliphatic structure of the CHOMg compositional space (A) for relevant loadings, which represent high (E) and low (G) thermal metamorphism signatures seen in the 61 meteorites studied. These plotted m/z values reflect the 50th percentile of the variables, which are unique for the positive (E) and negative (G) values of the first component (x axis) of the OPLS score plot (Fig. 5). These compounds in E may represent thermal metamorphism markers. The bubble size represents the relative intensity of the mass peaks. (F and H) Mass-edited H/C ratios of two representative examples for low- (Paris) and high-degree thermally processed meteorites (Soltmany) (35). Paris is known to be one of the least-altered meteorites (36). The convergence of O = 4 in CHOMg molecular formulas for thermal stress loading values is presented by an oxygen number- m/z diagram. (I) Again, these plotted m/z values reflect the 50th percentile of the variables, which are unique for the positive values of the first component (x axis) of the OPLS score plot (Fig. 5).

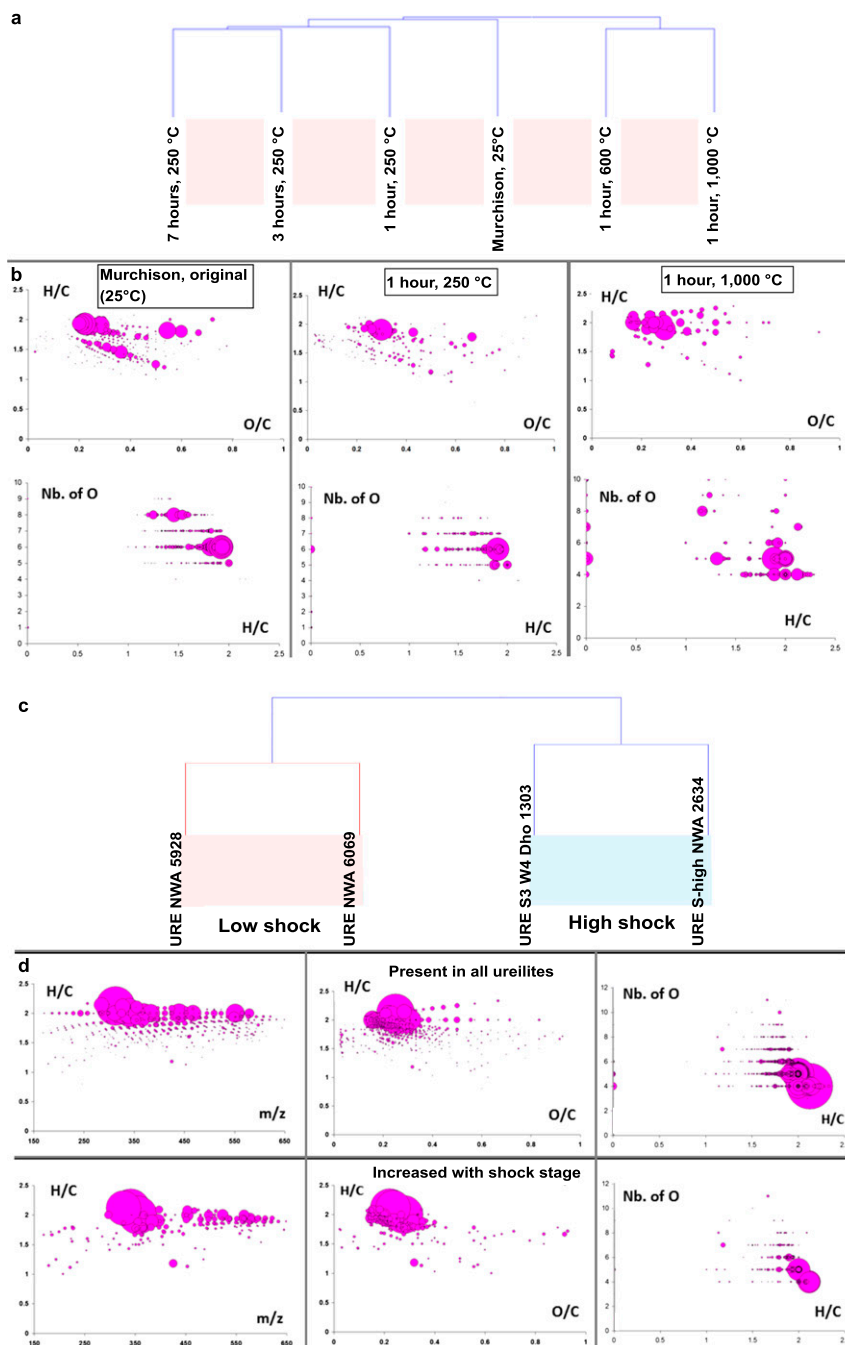


Fig. S7. Simulated thermal metamorphism of Murchison and CHOMg-based shock stage differentiation. (A) Laboratory experiment, in which a Murchison meteorite sample was heated to selected temperatures for variable durations (25 °C, 250 °C, 600 °C, and 1,000 °C). Number and distribution of organo-magnesium compounds enabled reconstruction of thermal exposure by means of HCA. The simulation of thermal metamorphism grades by increasing the temperature narrows the oxygen number in organomagnesium compounds to the MgO_4R^- class ($\text{R} = \text{hydrocarbon } \text{C}_x\text{H}_y$ and $x, y \in \mathbb{N}$), which dominates the entire CHOMg chemical space. This effect of convergence with increasing temperature is depicted in modified van Krevelen diagrams in *B*, resulting from negative ionization ESI-FT-ICR-MS data. The bubble size represents the relative intensity of the mass peaks. HCA organizes the samples, as a graphical output, into a dendrogram (cluster tree) whose branches are the desired clusters. Based on different similarity rules the clusters are defined. Similar samples are within a cluster. The samples clustered according their elevated temperatures (25 °C, 250 °C, 600 °C, and 1,000 °C). Sampling the effect of time-dependency on the variation of the CHOMg chemical space, three different time points were sampled for temperature 250 °C and clustered together. (C) Detailed differentiation of metamorphic states is illustrated, deduced from CHOMg-based HCA. Four ureilite meteorites were studied (NWA 5928, NWA 6069, Dhofo 1303, and NWA 2634), which had experienced high thermal and shock conditions (62). (D) (Top) CHOMg chemical spaces of four ureilite methanolic extracts (overlapped CHOMg compounds) are shown on top. (Bottom) CHOMg compositions, which increased in abundance in the higher-shocked ureilite meteorites Dhofo 1303 and NWA 2634.

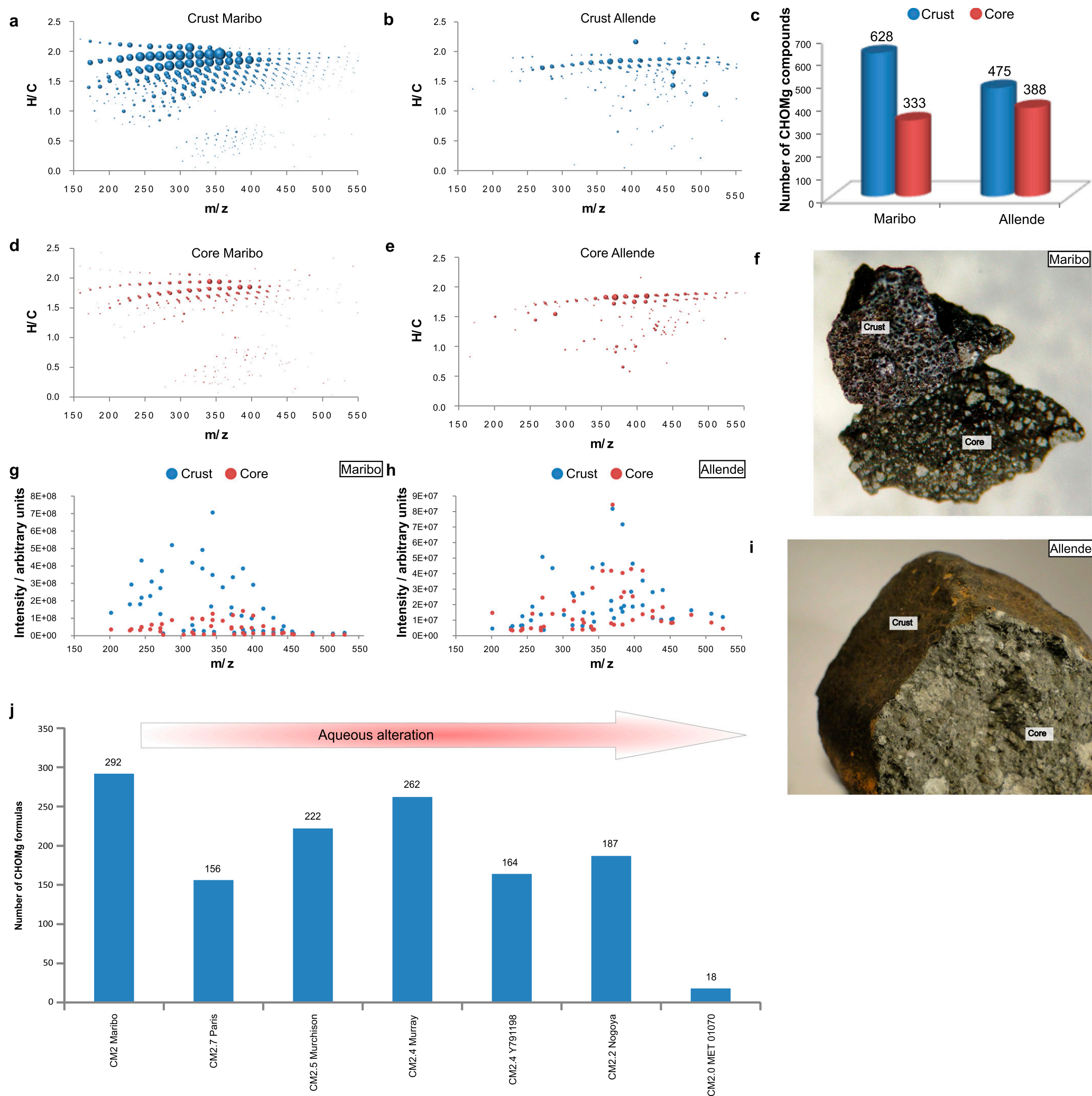


Fig. S8. Crust-core comparison and their influences on the CHOMg synthesis and dependency of CHOMg formulas on the aqueous alteration. (A) Number of CHOMg compounds in crust and core sections of the Maribo and Allende meteorites. The mass-edited H/C ratios (B–E) illustrate the increased coverage within the CHOMg chemical space for the crust, compared with the core (interior) region. Among the specific organomagnesium molecules, some are unique for the crust and for the core regions, respectively, indicative of a preferential spatial accumulation for certain CHOMg (F and G). The bubble size represents the relative intensity of the mass peaks. Pictures of the Maribo and the Allende specimens are shown in H and I, to reflect the different morphology of their outer crusts and their interiors. (J) Number of CHOMg molecular formulas in methanolic extracts of several CM2 meteorites that had been subjected to variable extents of aqueous alteration [classified from CM2.7 (left) to CM2.0 (right)]. No significant correlation between the extent of aqueous alteration of a meteorite and the number of organomagnesium compounds was retrieved, suggesting that the CHOMg synthesis is not directly dependent on the aqueous alteration.

Table S1. Information on 61 meteorite samples used in the statistical analysis

[Table S1](#)

Table S2. Coordinates of the relaxed geometry of C16-dihydroxymagnesium carboxylate complex anion (A), of C16-carboxylate anion (B), and of C5-dihydroxymagnesium carboxylate complex anion (C)

[Table S2](#)